

¹ To the Graduate Council:
² I am submitting herewith a thesis written by Jason Bane entitled “The EMC Effect
³ in A=3 Nuclei.” I have examined the final paper copy of this thesis for form and
⁴ content and recommend that it be accepted in partial fulfillment of the requirements
⁵ for the degree of Doctor of Philosophy, with a major in Nuclear Physics.

⁶
⁷

Nadia Fomin, Major Professor

⁸ We have read this thesis
⁹ and recommend its acceptance:

¹⁰ _____

¹¹ Jamie Coble

¹² _____

¹³ Kate Jones

¹⁴ _____

¹⁵ Thomas Papenbrock

¹⁶ _____

¹⁷ Soren Soreson

¹⁸

Accepted for the Council:

¹⁹
²⁰

Carolyn R. Hodges

²¹

Vice Provost and Dean of the Graduate School

²² To the Graduate Council:
²³ I am submitting herewith a thesis written by Jason Bane entitled “The EMC Effect
²⁴ in A=3 Nuclei.” I have examined the final electronic copy of this thesis for form and
²⁵ content and recommend that it be accepted in partial fulfillment of the requirements
²⁶ for the degree of Doctor of Philosophy, with a major in Nuclear Physics.

²⁷ Nadia Fomin, Major Professor

²⁸ We have read this thesis
²⁹ and recommend its acceptance:

³⁰ Jamie Coble

³¹ _____
³²

³³ Kate Jones

³⁴ _____
³⁵

³⁶ Thomas Papenbrock

³⁷ _____
³⁸

³⁹ Soren Soreson

⁴⁰ _____
⁴¹

⁴² Accepted for the Council:

⁴³
⁴⁴ Carolyn R. Hodges

⁴⁵ _____
⁴⁶

⁴⁷ Vice Provost and Dean of the Graduate School

⁴⁸ (Original signatures are on file with official student records.)

49

The EMC Effect in A=3 Nuclei

50

A Thesis Presented for

51

The Doctor of Philosophy

52

Degree

53

The University of Tennessee, Knoxville

54

Jason Bane

55

December 2018

⁵⁶

© by Jason Bane, 2018

⁵⁷

All Rights Reserved.

⁵⁸ Contents

⁵⁹	List of Tables	v
⁶⁰	List of Figures	vi
⁶¹	1 Introduction	1
⁶²	1.1 Electron scattering	2
⁶³	1.1.1 Deep inelastic scattering	5
⁶⁴	1.2 EMC Effect	6
⁶⁵	1.3 MARATHON	9
⁶⁶	2 Experimental Setup	10
⁶⁷	2.1 Thomas Jefferson Lab	10
⁶⁸	2.1.1 CEBAF	10
⁶⁹	2.1.2 Hall A	12
⁷⁰	2.2 Target	17
⁷¹	2.3 High Resolution Spectrometers	19
⁷²	2.3.1 Vertical Drift Chambers	20
⁷³	2.3.2 Scintillators	22
⁷⁴	2.3.3 Cherenkov	22
⁷⁵	2.3.4 Shower Calorimeter	22
⁷⁶	2.3.5 Pion Rejector	22
⁷⁷	2.3.6 FPP Chambers	22

78	2.4 Trigger Setup	22
79	2.5 DAQ - Data Acquisition System	22
80	2.6 Kinematic Settings	22
81	3 Calibration	23
82	3.1 Beam Line	23
83	4 Data Analysis	26
84	4.1 Efficiencies	26
85	4.1.1 Particle Identification Efficiency	26
86	5 Results	30
87	6 Simulation	31
88	6.1 Investigation	31
89	6.2 Transformation	32
90	6.3 Results	34
91	7 Conclusion	37
92	Bibliography	38

⁹³ **List of Tables**

⁹⁴ List of Figures

⁹⁵	1.1	Simple Feynman diagram of an electron scattering from a proton [7].	3
⁹⁶	1.2	Graph of the ratio of A/D structure functions vs x for Carbon [10].	7
⁹⁷	1.3	EMC effect from EMC, SLAC, and BCDMS [17]	8
⁹⁸	1.4	Graph of the ratio of A/D structure functions vs x for Carbon [10].	9
⁹⁹	2.1	Schematic Layout of CEBAF.	11
¹⁰⁰	2.2	A 3D drawing of Hall A.	12
¹⁰¹	2.3	A schematic layout of the beam line in Hall. [1]	13
¹⁰²	2.4	BPM design diagram, from JLab instrumentation group. Beam direction is from left to right [23].	14
¹⁰⁴	2.5	BPM design diagram, looking down the beam line[23].	14
¹⁰⁵	2.6	Hall A Current Monitor components [4].	16
¹⁰⁶	2.7	Target Images	18
¹⁰⁷	2.8	A side view of a HRS [1].	20
¹⁰⁸	2.9	A view of both the left(top) and right(bottom) detector stacks inside the left and right HRS [1].	21
¹¹⁰	2.10	A sketch of the two VDC planes in the HRSs with a particle traveling through the detector at 45° .[6].	22
¹¹²	3.1	A schematic layout of a harp fork [23]	24
¹¹³	3.2	The X and Y position for a Bulls eye scan for BPM calibration.	25

114	4.1	Two dimensional plot of the cherenkov sum versus Total Energy de-		
115		posited, including electron sampling in teal and non-electron sampling		
116		in red.		27
117	4.2	Electrons and other back ground particles identified via cuts in the total		
118		calorimeter and the gas cherenkov shown in the individual layers of the		
119		calorimeters. Sampling cuts for Electrons in teal and Non-Electrons in		
120		red.		28
121	4.3	Electrons and other back ground particles identified via cuts in the		
122		total calorimeter and the gas cherenkov shown in the sum of the gas		
123		cherenkov.Sampling cuts for Electrons in teal and Non-Electrons in red.	29	
124	6.1	Example of the electron beam(red) with a energy of 2.5 GeV and the		
125		proton(blue) with angle of 45° in respect to the electron and with a		
126		momentum of 0.5 GeV/c.		32
127	6.2	Vector representations of the momentum for the incoming electron(red)		
128		and target proton(blue) with units of GeV for each phase of their		
129		transformations before scattering.		33
130	6.3	Vector representations of the momentum for the incoming electron(red)		
131		and target proton(blue) with units of GeV for each phase of their		
132		transformations after scattering).		35
133	6.4	Simulation results for fixed momentum protons. Three runs with		
134		unique proton momentum.		36

₁₃₅ **Chapter 1**

₁₃₆ **Introduction**

₁₃₇ Understanding the world around us is the goal of every scientist, from the chemist
₁₃₈ that experiments with the formation of atoms to the geologist exploring the process of
₁₃₉ rock formations. Nuclear physicists focus on studying the fundamental constituents
₁₄₀ of matter, the building blocks of nature. Physicist use scattering experiments at
₁₄₁ accelerator facilities, like CERN in Switzerland, DESY in Germany, BATES in
₁₄₂ Massachusetts, JLAB in Virginia, and many others, to study the protons and neutrons
₁₄₃ and their constituents that make up a nucleus. These experiments allow physicists
₁₄₄ to observe the internal structure of the nucleus and to investigate the interactions
₁₄₅ between the quarks and gluons. Many of the experiments are design to confirm a
₁₄₆ existing results while also expanding on unique ideas.

₁₄₇ In the last century, there have been numerous breakthroughs in the fields of nuclear
₁₄₈ and particle physics. Rutherford discovered the proton by bombarding light nuclei
₁₄₉ with alpha particles to produce



₁₅₀ This reaction allowed Rutherford to conclude that the Hydrogen nucleus was a
₁₅₁ constituent of an atomic nuclei [18]. In the late 1950s, experimental results published

152 by W. McAllister and R. Hofstadter exposed some of the eternal structure of the
153 proton [7, 15]. The European Muon Collaboration(EMC) produced results in the
154 early 1980s showing a differences between the internal structure of the deuterium
155 nucleus and Iron [20, 10]. The data received from scattering experiments using alpha
156 particles contain information about the target, the beam, and the interaction between
157 the two. Deciphering and analyzing this data can be convoluted because the cross-
158 section contains information about the internal structure of the target and the beam
159 along with the interaction and forces between the two [18].

160 1.1 Electron scattering

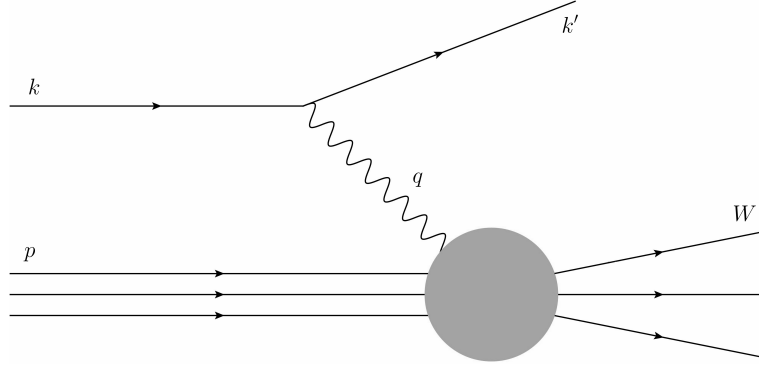
161 In order to remove some of the complexity in scattering experiments, one may
162 employ highly relativistic electrons. Electrons being point-like particles without any
163 internal structure allow the elimination of some of the analysis difficulties with using
164 alpha particles in scattering experiments due to their complex internal structure.
165 Electrons and the target nucleus, nucleon, or quarks interact via the exchange of
166 a virtual photon. Using quantum electrodynamics (QED), these interactions can
167 accurately be described by the well known electromagnetic interaction. Higher order
168 terms of this process contribute very little due to the coupling constant $\alpha \approx 1/137$,
169 being much smaller than one.

170 Figure 1.1 represents an electron scattering from a proton. The incoming or incident
171 electron's four-momentum is described as $k = (E, \vec{k})$ and the scattering electron's four-
172 momentum is represented by $k' = (E', \vec{k}')$. The exchange of the virtual photon in this
173 electromagnetic interaction is defined by the four-momentum transfer q :

$$Q^2 \equiv -q^2 = 4EE' \sin^2(\theta/2). \quad (1.2)$$

₁₇₄ In equation 1.2, E and E' are the electron energy before and after the scattering
₁₇₅ interaction. Theta is the angle that describes the deflection of E' from the electron's
₁₇₆ original path.

Figure 1.1: Simple Feynman diagram of an electron scattering from a proton [7].



₁₇₇ Along with Q^2 , the variables ν , W , and x_B are used to narrate the evolution of the
₁₇₈ electron scattering process. ν , defined as $p \cdot q/M$. In the rest frame of the target, ν
₁₇₉ can be described by:

$$\nu = E - E'. \quad (1.3)$$

₁₈₀ Simply, ν is the magnitude of energy loss by the electron during the scattering
₁₈₁ interaction. The invariant mass of the system, W , defines the hadronic state produced
₁₈₂ by the scattering event.

$$W^2 \equiv (q + p)^2 = M^2 + 2M\nu - Q^2. \quad (1.4)$$

₁₈₃ A scattering event with the invariant mass equal to the square of the mass of the
₁₈₄ nucleon, (M^2), falls in the regime of elastic scattering. W above M^2 will transform
₁₈₅ the scattering interaction from an elastic scattering to inelastic scattering due to
₁₈₆ the excited state of the scattered byproduct. x_B , the Bjorken scaling variable is a
₁₈₇ dimensionless quantity that measures the inelastically of a scattering process. x_B is
₁₈₈ defined as: $x := \frac{Q^2}{2M\nu}$.

189 The intrinsic likelihood of an event with a certain Q^2 , ν , and W is defined by the
 190 scattering cross section. An electron scattering off of a target with a charge of $Z * e$
 191 can be described by the Rutherford cross-section. Povh et. al. details the Rutherford
 192 cross section as:

$$\left(\frac{d\sigma}{d\Omega} \right)_{Rutherford} = \frac{(zZe^2)^2}{(4\pi\epsilon_0)^2 * (eE_{kin})^2 \sin^4(\theta/2)}. \quad (1.5)$$

193 In the early 1920s, German physicists Stern and Gerlach performed an experiment
 194 that confirmed the presence of electron angular momentum. Later a discovery of
 195 electron spin was made by Uhlenbeck and Goudsmit. The Rutherford cross-section
 196 neglects the spin of an electron and its target. The Mott cross-section is the evolved
 197 version of the Rutherford cross-section. It has been modified to include the intrinsic
 198 spin of the target and electron. The Mott cross-section is: [12, 18]

$$\left(\frac{d\sigma}{d\Omega} \right)_{Mott} = \frac{4Z^2\alpha^2(\hbar c)^2 E'^2}{|\mathbf{q}_c|^4} \cos^2(\theta/2). \quad (1.6)$$

199 There is an agreement between the measured cross section and the theoretical Mott
 200 cross-section when in the limit of $|\mathbf{q}| \rightarrow 0$ for scattering events of electrons off of a
 201 target nuclei. As $|\mathbf{q}|$ climbs further from zero, the experimentally measured cross
 202 sections systematically decreases [18]. Increasing the $|\mathbf{q}|$ of an interaction reduces
 203 the size of the wavelength of the virtual photon that mediates the electromagnetic
 204 interaction between the electron and target nuclei and increases the resolution of the
 205 probe. The wavelength of this virtual photon is inversely proportional to $|\mathbf{q}|$, and can
 206 be described by the following: $\lambda = \frac{\hbar}{|\mathbf{q}|}$ [18]. Increasing the amount of momentum
 207 transferred in an electromagnetic reaction allows one to study deeper into the nucleus.

208 Studying the internal structure of a nucleus with the electromagnetic interaction
 209 requires increasing the momentum transferred. Pushing $|\mathbf{q}|$ to be comparable with the
 210 mass of a nucleon adds more complexity to the details of the scattering interaction.

211 At the appropriate levels of $|\mathbf{q}|$ to study the nucleons in the nucleus, the Mott cross-
 212 section equation requires modifications to include additional factors that incorporate
 213 information about the target. The Rosenbluth formula is based on the Mott
 214 cross section and embraces target recoil, magnetic moment, and charge and current
 215 distributions. Povh writes the Rosenbluth formula as:

$$\left(\frac{d\sigma}{d\Omega}\right) = \left(\frac{d\sigma}{d\Omega}\right)_{Mott} * \left[\frac{G_E^2(Q^2) + \tau G_M^2(Q^2)}{1 + \tau} + 2\tau G_M^2(Q^2) \tan^2 \frac{\theta}{2} \right]. \quad (1.7)$$

216 Equation 1.7 contains $G_E^2(Q^2)$ and $G_M^2(Q^2)$, the electric and magnetic form factors. τ
 217 is used in the Rosenbluth formalism to account for the magnetic moment of a nucleon
 218 and is defined as: $\tau = \frac{Q^2}{4M^2c^2}$ [18]. In the general case of electron scattering off of a free
 219 proton or neutron elastically, the scattered energy of the electron will be a function
 220 of the incident electron's energy and the scattered angle of the electron, shown in the
 221 following equation.

$$E' = \frac{E}{1 + \frac{E}{Mc^2}(1 - \cos\theta)} \quad (1.8)$$

222 1.1.1 Deep inelastic scattering

223 The first generation of electron scattering experiments achieving a significantly
 224 large $|\mathbf{q}|$ used a linear accelerator with a 25 GeV maximum beam energy, and
 225 following generations increased the total interaction energy to substantially higher
 226 thresholds. At these high incident beam energies, individual resonances cannot be
 227 separated in the invariant mass spectrum above 2.5 GeV. Observations made into
 228 this convoluted invariant mass spectrum has shown that many strongly interacting
 229 particles are produced, known as hadrons. Scattering interactions that generate
 230 these hadrons are considered to be inelastic. Inelastic scattering events contain
 231 the possibility of conceiving additional resultants and increase the complexity of
 232 a scattering interaction. Inelastic scattering events occur when the wavelength
 233 of the virtual photon is comparable to the radius of the struck nucleon or when
 234 $Q^2 R^2 \lesssim 1$ [18]. Increasing the amount of transferred momentum so that $Q^2 R^2 \gtrsim 1$,

235 increase the resolution of the probe to a level that allows for the interacting with
 236 the charge constituents within the nucleon. When the scattering event probes the
 237 fundamental elements of a nucleon, the scattering process is titled deep inelastic
 238 scattering(DIS). Due to the increase in complexity, an additional degree of freedom
 239 has to be introduced into the scattering cross section equation. Modifying the
 240 Rosenbluth formula to include the inelastic scattering structure functions $F_1(Q^2, \nu)$
 241 and $F_2(Q^2, \nu)$ evolves the Rosenbluth formula to contain the needed complexity of an
 242 inelastic event. These modifications are shown in equation 1.9.

$$\frac{d^2\sigma}{d\Omega dE'} = \left(\frac{d\sigma}{d\Omega} \right)_{Mott} \left[\frac{F_2(Q^2, \nu)}{\nu} + \frac{2F_1(Q^2, \nu)}{M} \tan^2 \frac{\theta}{2} \right] \quad (1.9)$$

243 The F_1 and F_2 structure functions provide the details for describing the internal
 244 composition of the nucleon [18].

$$F_2(x) = x \mathbf{1} \cdot \sum_f z_f^2 (q_f(x) + \bar{q}_f(x)) \quad (1.10)$$

245 [21] [13]

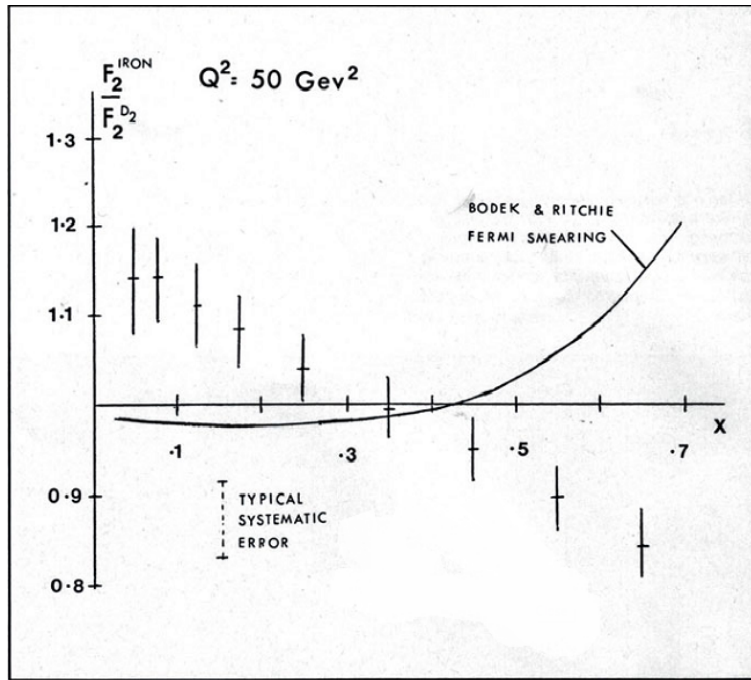
246 1.2 EMC Effect

247 The European Muon Collaboration (EMC) performed a deep inelastic measurement
 248 with 120-280 GeV muons on iron and deuteron targets [14]. The EMC extracted A/D
 249 structure function ratios versus the Bjorken scaling variable, x . The relationship
 250 originally expected by the EMC contained the sum of the structure functions of each
 251 nucleon in a nucleus. Each nucleus has a certain number of neutrons (N) and a amount
 252 of protons (Z). The expected structure function for a nucleus could be written as:

$$F_A = N F_2^N + Z F_2^P. \quad (1.11)$$

253 The EMC compared the extracted structure functions from iron and deuterium.
 254 Their results are shown in Figure 1.2. The $\frac{A}{D}$ structure function ratio showed
 255 an unexpected downward slope. This phenomenon was titled the EMC effect.
 256 This finding demonstrated to the EMC that their understanding of the nucleus
 257 was incorrect. A nucleon's structure function and thereby, the constituent quark
 distributions may be altered by the nucleus.

Figure 1.2: Graph of the ratio of A/D structure functions vs x for Carbon [10].

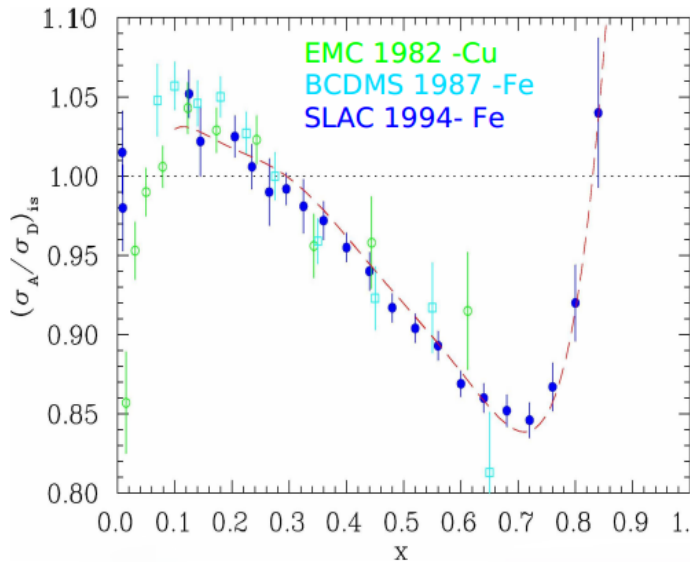


258

259 Ever since the European Muon Collaboration discovered the depletion of quarks at
 260 high x for $A > 2$ nuclei, physicists have tried to discover its cause. Scientists at SLAC
 261 extracted structure function ratios for many nuclei including; ${}^4\text{He}$, ${}^9\text{Be}$, ${}^{12}\text{C}$, ${}^{27}\text{Al}$,
 262 ${}^{40}\text{Ca}$, ${}^{56}\text{Fe}$, ${}^{108}\text{Ag}$, and ${}^{197}\text{Au}$. There were slightly different results for each nucleus.
 263 The magnitude of the EMC effect, taken to be the A/D ratio at $x = 0.6$, was found
 264 to be different for the various nuclei, and roughly scaled with the size or density of
 265 the nuclei. The NMC (New Muon collaboration), another group at CERN, gathered
 266 precise data in order to construct the inclusive cross section of deuterium and protons.

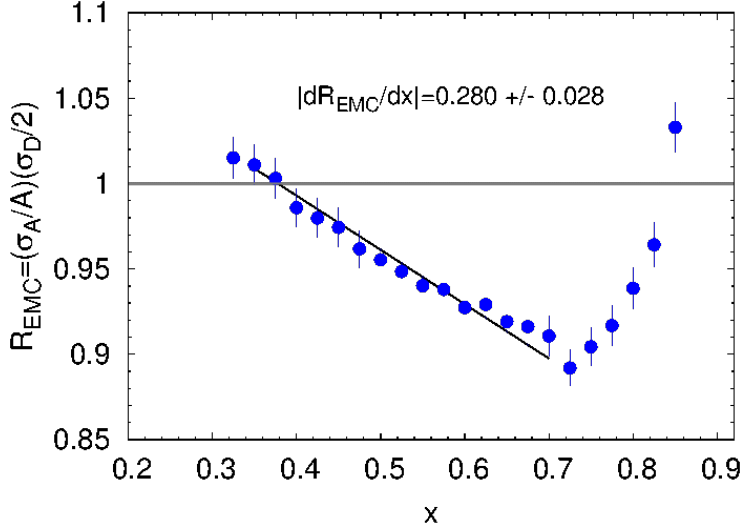
267 BCDMS collaboration extracted data for N and Fe structure function ratios. Figure
 268 1.3 shows some of the data from SLAC and BCDMS on the EMC effect for Iron
 269 and Cu. Figure 1.4 shows this result from a recent JLab EMC measurement, most
 270 precise to date. Many models over the years have been able to reproduce the shape
 271 of the A/D ratios. These models can contain traditional nuclear physics effects like
 272 momentum distribution or pion-charge contributions. Some models also describe the
 273 EMC effect through quark momentum distribution or modification of the internal
 274 structure [17, 5, 2, 8, 9]. However, no single model has provided a complete picture
 275 of the possible underlying physics. Precise data from Jlab's E03-103 experiment has
 276 revitalized this research. This experiment focused on precision measurements in light
 277 nuclei and added ${}^3\text{He}$ as a target nucleus. Instead of taking the A/D ratio at a
 278 certain x -value to be the magnitude of the EMC effect, this analysis looked at the
 279 slope instead. This eliminated sensitivity to normalization uncertainties.

Figure 1.3: EMC effect from EMC, SLAC, and BCDMS [17]



280 In Figure , ${}^9\text{Be}$ was found not to follow the previously observed scaling with
 281 nuclear density. This result from Jefferson Lab determined that the previous idea

Figure 1.4: Graph of the ratio of A/D structure functions vs x for Carbon [10].



of a dependence on A or nuclear density in the EMC effect to be incorrect [20]. This result spawned a drive to determine another explanation for the EMC effect and understand what clue the ${}^9\text{Be}$ outlier was providing. The structure of this nucleus is made up of two high-density alpha particles and a single neutron [3]. The regions of higher density that are contained in a comparatively large volume may be able to explain why ${}^9\text{Be}$ does not follow the expected trend. This suggests that the EMC effect could be a function of local nuclear density [20].

1.3 MARATHON

Experiment E12-010-102, MARATHON (MeAsurement of the $F2^n/F_2^p, d/u$ RAtios and A=3 EMC Effect in Deep Inelastic Electron Scattering Off the Tritium and Helium MirOr Nuclei), will use deep inelastic scattering off of the mirror nuclei ${}^3\text{H}$ and ${}^3\text{He}$ to measure the EMC effect for both ${}^3\text{H}$ and ${}^3\text{He}$, to determine the ratio of the neutron to proton inelastic structure functions, and to find the ratio of the down to up quark distributions in the nucleon.

296 **Chapter 2**

297 **Experimental Setup**

298 **2.1 Thomas Jefferson Lab**

299 Thomas Jefferson Lab (Jlab) in Newport News, Virginia hosted the MARATHON
300 experiment in the Fall of 2017 and Spring of 2018. Jlab uses support from the U.S.
301 Department of Energy(DOE) and the state of Virgina to complete the lab's mission of
302 delivering productive research by exploring the atomic nucleus and its fundamental
303 constituents, including precise tests of their interactions. Along with applying an
304 advanced particle accelerator, particle detectors and other technologies to develop
305 new basic research capabilities and to address the challenges of a modern society.

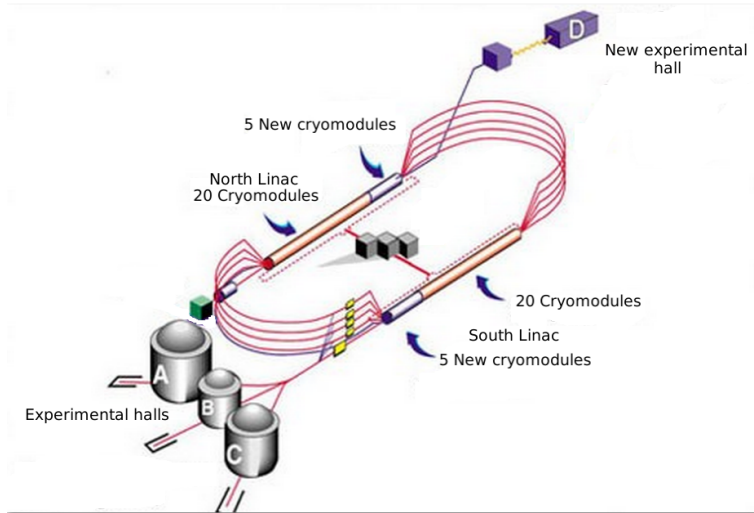
306 **2.1.1 CEBAF**

307 The Continuous Electron Beam Accelerator Facility (CEBAF) was recently
308 upgraded to a 12 GeV accelerator, upgrading it to be able to supply a 11 GeV beam
309 of continuous electrons of up to $200 \mu\text{A}$ of current to three experimental halls (A,B,C)
310 and 12 GeV to the recently constructed hall D. After being accelerated to 45 MeV by
311 a polarized electron gun or a thermionic injector, the electrons are injected into the
312 North linear accelerator (LINAC), shown in figure 2.1. The polarized gun can supply
313 electrons with up to 80% polarization and the polarization direction can be controlled

³¹⁴ by a wien filter. To ensure the level of polarization, a 5 MeV Mott polarimeter may
³¹⁵ be used to measure the level of polarization[1].

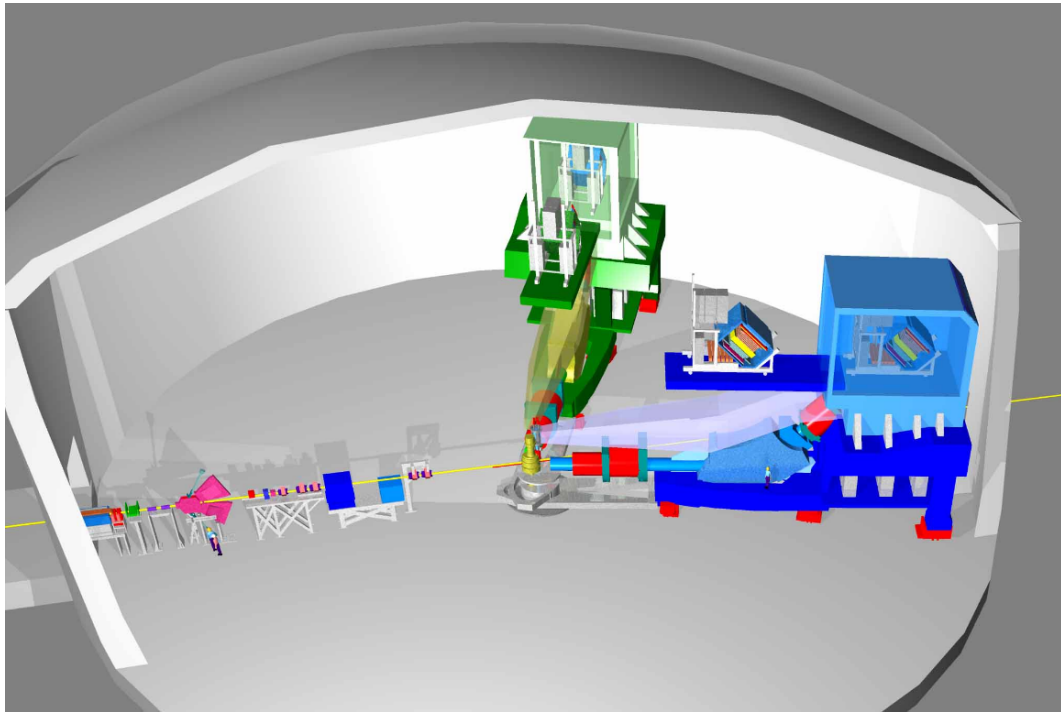
³¹⁶ The electrons are conveyed through two LINACs and two bending arcs per complete
³¹⁷ pass of the accelerator. Electrons traveling to Halls A, B, and C complete a maximum
³¹⁸ of four and a half revolutions around the accelerator. Electrons going to all D travel
³¹⁹ through the north LINAC for an extra boost. These particles receive approximately
³²⁰ 2.2 GeV in energy for each cycle through the accelerator. The radio frequency (RF)
³²¹ cavities in each LINAC use an oscillating electromagnetic field to supply a force to
³²² accelerate the passing electrons. These Niobium RF cavities are cooled to 2 K in
³²³ order to create conditions that allow the cavities to be superconducting [1].

Figure 2.1: Schematic Layout of CEBAF.



³²⁴ **2.1.2 Hall A**

Figure 2.2: A 3D drawing of Hall A.

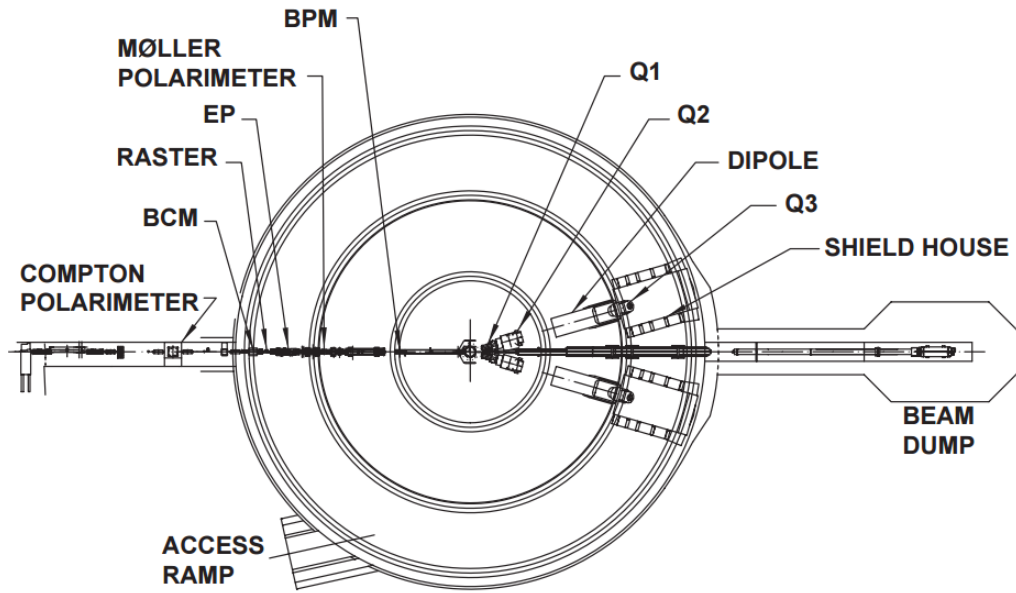


³²⁵ The experimental Hall A and the scientific equipment used were designed for
³²⁶ detailed investigations of the internal structure of nuclei. Two high resolution
³²⁷ spectrometers in Hall A use the inclusive (e,e') and exclusive $(e,e' p)$ reactions to gain
³²⁸ a greater understanding of the structure of the nucleus. Completing detailed studies
³²⁹ with high resolution and extreme accuracy requires knowing the beam position, size,
³³⁰ energy, current, direction, and polarization when the beam strikes the target. The
³³¹ instrumentation used in the precise measurement of these quantities in Hall A are
³³² shown in figure 2.3 [1].

³³³ A pair of Beam Position Monitors(BPM)s are used to measure the relative beam
³³⁴ position without affecting the beam. The two Hall A BPMs are located at 7.524 m
³³⁵ and 1.286 m away from the target. Using the standard difference-over-sum technique,
³³⁶ the relative beam position is determined with an accuracy of 100 μm with a beam

337 current of at least $1 \mu\text{A}$ [1]. The BPMs' positional data is recorded in two ways.
 338 Every second of beam time, the beam position average over 0.3 seconds is logged
 339 into the Experimental Physics and Industrial Control System (EPICS) database.
 340 The BPMs also transmit data event-by-event to the CEBAF online Data Acquisition
 341 system(CODA).

Figure 2.3: A schematic layout of the beam line in Hall. [1]



342 The main beam line components of the BPMs consist of four open-ended antennas.
 343 Figure 2.4 shows a BPM chamber and figure 2.5 shows the layout of the four antennas
 344 as you look down the beam line. In this chamber, the design of three of the four
 345 antennas can be seen. The antennas are titled u_+ , u_- and v_+ , v_- . The antennas
 346 receive an induced signal as electrons pass to determine the beam position in the
 347 u and v directions. The direction of the beam is determined by using the two
 348 BPMs in conjunction with timing information provided. The accuracy of the BPMs
 349 requires an absolute measurement of the electron beam's position to calibrate the
 350 BPMs and a internal input oscillation measurement names twiddle to supply BPM
 351 signal coefficients. [19, 23].

Figure 2.4: BPM design diagram, from JLab instrumentation group. Beam direction is from left to right [23].

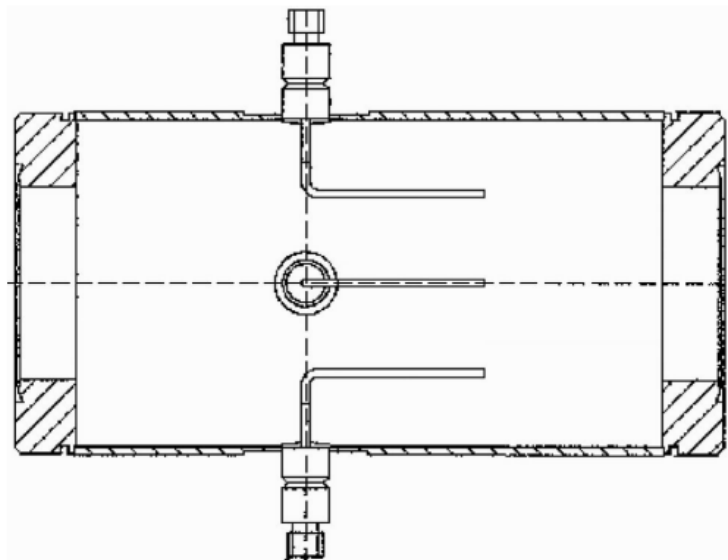
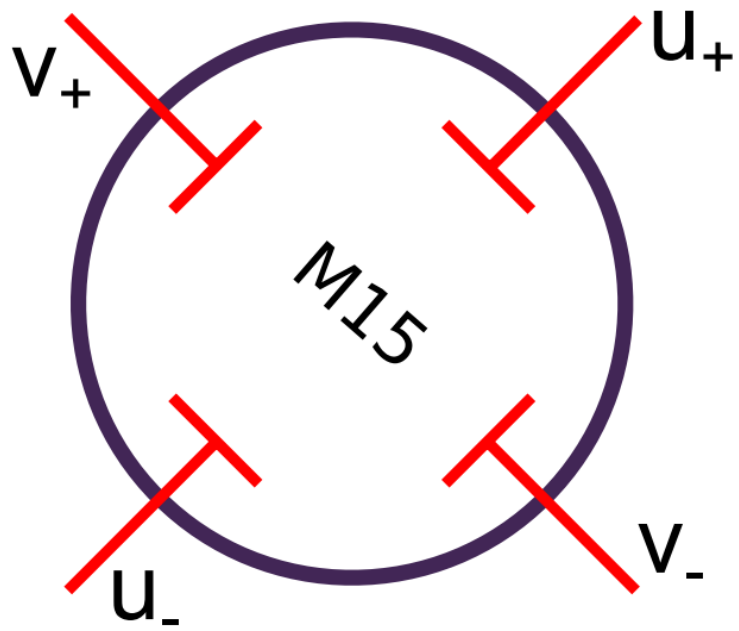


Figure 2.5: BPM design diagram, looking down the beam line[23].



352 Damage to a target system from intense beam can cause extreme fluctuations in
353 the target's temperature and density. A raster was used to counteract the damage

354 caused by a focused beam. The raster used two magnetic fields produced by two
355 dipoles to spread the electron beam out. This produces a large rectangle interaction
356 area on the front face of the target container. A triangle wave of 25 kHz was used to
357 control the coils of the dipole magnets. The raster systems are located \approx 17 meters
358 before the target chamber (upstream of the target[23]). The rasters position can be
359 seen in figure 2.2. Safety constraints administrated by the target group at JLAB
360 limited the minimum size of the raster spot for the MARATHON experiment to two
361 millimeters by two millimeters. This limit was installed has a safety concern for the
362 tritium target.

363 The Hall A raster system consists of four dipoles. Two dipoles produce magnetic
364 fields in the horizontal direction of the lab frame and two in the vertical. The upstream
365 raster and downstream rasters include one vertical and one horizontal dipole. The
366 relative change in position of the incoming electrons are controlled by the current
367 supplied to the dipoles. In order to obtain the change in beam position due to the
368 rasters, a calibration between the raster current and measured beam position were
369 obtained.

370 The electron beam energy is located in many of the equations used in an electron
371 scattering experiment. This can cause a noticeable increase in systematic error if the
372 beam energy measurement is not made precisely. At JLAB for the MARATHON
373 experiment, the beam energy was measured in two ways. In Hall A, the beam energy
374 was measured by using the (e,e/p) method. On the beam line, 17 meters upstream
375 from the target an ep scattering chamber is located. The beam was directed into the
376 target containing a rotating 10-30 μm thick tape of CH_2 . The scattering angle of the
377 electron and the recoil angle of the proton are used to determine the beam energy
378 using equation 2.1. Where M_p is the mass of the proton and θ_p, θ_e are the scattered

³⁷⁹ angle of the proton, electron respectively.

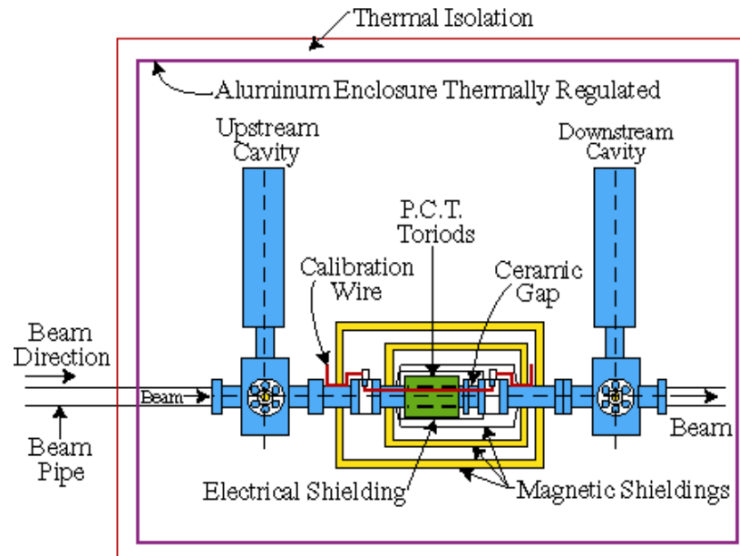
$$E = Mp \frac{\cos\theta_e + \frac{\sin\theta_e}{\tan\theta_p} - 1}{1 - \cos\theta_e} \quad (2.1)$$

³⁸⁰ The beam energy was also measured using the ark measurement method [7]. This
³⁸¹ method uses changes in beam position and precise measurements of the magnetic
³⁸² fields around the beam line to determine the energy of the electron beam. The angle
³⁸³ at which the electrons are bent through is related to the momentum of the electrons,

$$p = k \frac{\int \vec{B} \cdot d\vec{l}}{\theta}. \quad (2.2)$$

³⁸⁴ In equation 2.2, p is the momentum of the electrons, θ is the bend angle, and \vec{B}
³⁸⁵ is the magnetic field the electron experiences. Then using the momentum of the
³⁸⁶ electron, the energy of the beam can be extracted. The error on the beam energy
³⁸⁷ measurement is $\delta E/E \approx 2 * 10^{-4}$ [22, 7]. The MARATHON experiment used both
³⁸⁸ methods to accurately determine the electron beam energy.

Figure 2.6: Hall A Current Monitor components [4].



389 The main process of measuring the scattering yield for a calculation of a cross
390 section looks at finding the ratio of the number of electrons scattered to the number
391 of electrons sent. In order to accurately determine the number of electrons sent to
392 scatter with our target system, Hall A use a highly accurate and non-invasive beam
393 current monitor(BCM). The Hall A BCM has an absolute accuracy of 0.2 percent
394 as long as the current is between 1 and 180 μ A. The BCM used in Hall A consists of
395 three main components: a Parametric Current Transformer (PCT) and two pill box
396 cavities. Figure 2.6 shows the components in the Hall A BCM. The BCM produces
397 an RF signal that is proportional to the beam current. An 10 kHz down converter,
398 RMS-to-DC converter, voltage-to-Frequency converter, and a scaler are used to inject
399 the current signal into the Hall A DAQ. Proportionality constants are determined in
400 the calibration process to correctly integrate the charge for a given amount of beam
401 current[4]. Continue after the initial beam line components, an electron will enter
402 into the target chamber, housing the target system.

403 2.2 Target

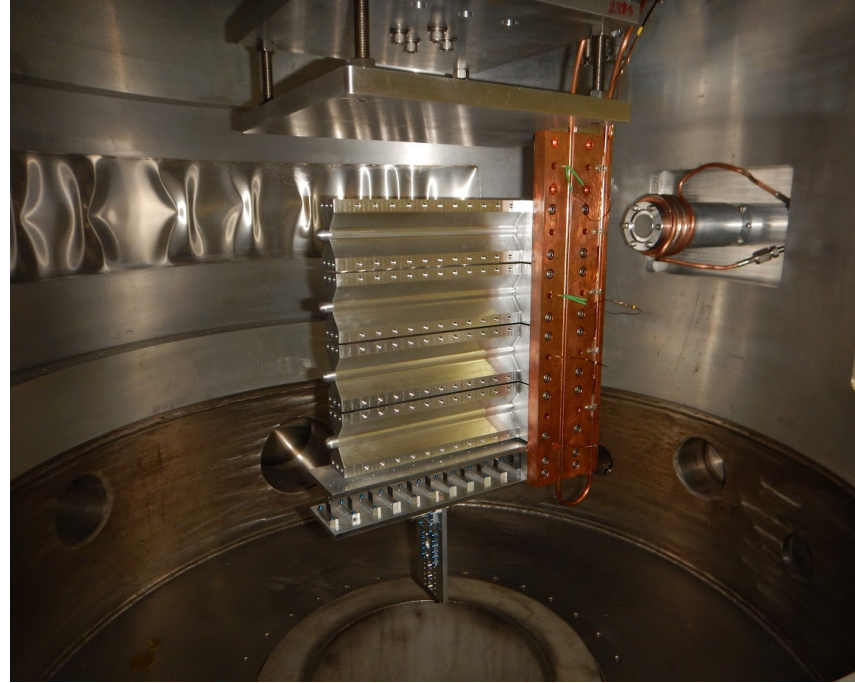
404 The Hall A Tritium Target(HATT) system was used for the Tritium run group of
405 experiments. The HATT target chamber was repurposed from a previously used cryo-
406 target chamber in order to reduce the financial cost of designing a new target chamber.
407 The refurbishing of the cryo-target chamber consisted of adding in new safety features
408 to prevent and mitigate a tritium leak. A 4 inch long collimator with an inner diameter
409 of 0.4 inch was added inside of the target chamber but upstream of the target ladder
410 to prevent the beam from striking the thin side wall of the aluminum cell. In case of
411 a tritium leak in the target chamber, an exhaust system was installed to control the
412 amount of tritium exposed to the Hall.[16] Figure 2.7 shows the HATT system with
413 the target ladder in the home position and the scattering windows removed. A picture
414 of the HATT ladder installed in the HATT system is shown if figure 2.7. The ladder
415 contains both gaseous cells and solid targets. The MARATHON experiment had five

Figure 2.7: Target Images

(a) A image of the HATT. [11]



(b) Image of the Hall A Tritium Target Ladder. [11]



416 gas cells. The top four of the gas cells were filled with tritium, deuterium, hydrogen,
417 and $^3\text{helium}$, from top to bottom respectively. Due to safety restricts the tritium
418 cell was not installed until the HATT system could be closed. The bottom most
419 cell was left empty, to complete end cap subtractions. The lower half of the target
420 ladder contains the solid targets used during the MARATHON experiment. Listed
421 from top to bottom, the solid targets used were a pair of thick aluminum foils, carbon
422 multifoil, single carbon foil, and a carbon foil with a 2mm diameter hole. The thick
423 Al foils were used to aid the target window background subtraction. The multifoil
424 target also know has the optics target was used to calibrate the z-axis reconstruction
425 of the optics matrix. The single carbon foil and carbon hole were used to calibrate
426 the BPMs and rasters and to determine the off set of the central line of the detector.

427 2.3 High Resolution Spectrometers

428 Electrons that successfully scatter from the target may end up in either of the two
429 HRSs(High Resolution Spectrometers). The HRSs were designed to detect charged
430 particles with a high degree of precision. In order to achieve a high level of resolution
431 in momentum and angle, the HRSs were designed with a magnet configuration of
432 QQD_nQ (quadrupole, quadrupole, dipole, and quadrupole). The vertical bending
433 dipole provides the field required to transport the scattered particles through the
434 45° bending angle to the detector hut. A drawing of an HRS can be seen in
435 figure 2.8. The first quadrupole(Q1) focuses the incoming electrons in the vertical
436 plane. The following two quadrupoles (Q2 and Q3 provide transverse focusing. This
437 optical design allows the use of extended gas targets with no substantial loss in solid
438 angle[1]. The spectrometers were designed to perform various functions which include:
439 triggering the data acquisition system (DAQ) when certain requirements are met,
440 gathering the position and direction of individual particles to reconstruct a track,
441 provide precise timing information for time of flight calculations, and identify many
442 different particle types that pass through the detector system. In order for both
443 the Left HRS (LHRS) and Right HRS (RHRS) to complete the required task, they
444 contain a myriad of detectors. The HRSs use drift chambers, scintillators, cerenkov
445 detectors, and shower calorimeters. Both the Left and Right HRSs contain two planes
446 of scintillators to function has the main trigger for the detector package. The vertical
447 drift chambers (VDC) that lay at the front of the detector in conjunction with the
448 Shower that lies in the back of the detector provide information for reconstructing the
449 particle tracks and precise timing. Particles are identified by the cerenkov, shower
450 calorimeters, and pion rejectors that are contained in the left or right HRS. The
451 layout of the individual detectors that make up the left and right detector package
452 are shown in figure 2.9 [1].

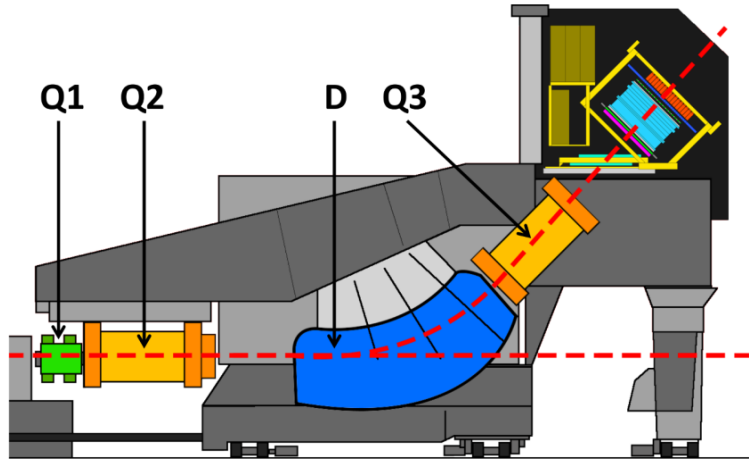


Figure 2.8: A side view of a HRS [1].

453 2.3.1 Vertical Drift Chambers

454 Each of the spectrometers housed in Hall A contains a vertical drift chamber(VDC).
 455 Each VDC contains two planes of crossing sense wires. Shown in figure 2.10, the two
 456 planes of the VDC lie a distance of 0.335m apart [6]. The lower plane of the VDC
 457 is positioned at the approximate focal plane of the HRS and lies in the horizontal
 458 plane of the Hall A coordinate system. The sense wires located in the VDCs cross
 459 orthogonally. They are offset by 45° in respect to the dispersive and non-dispersive
 460 directions.

461 [6]

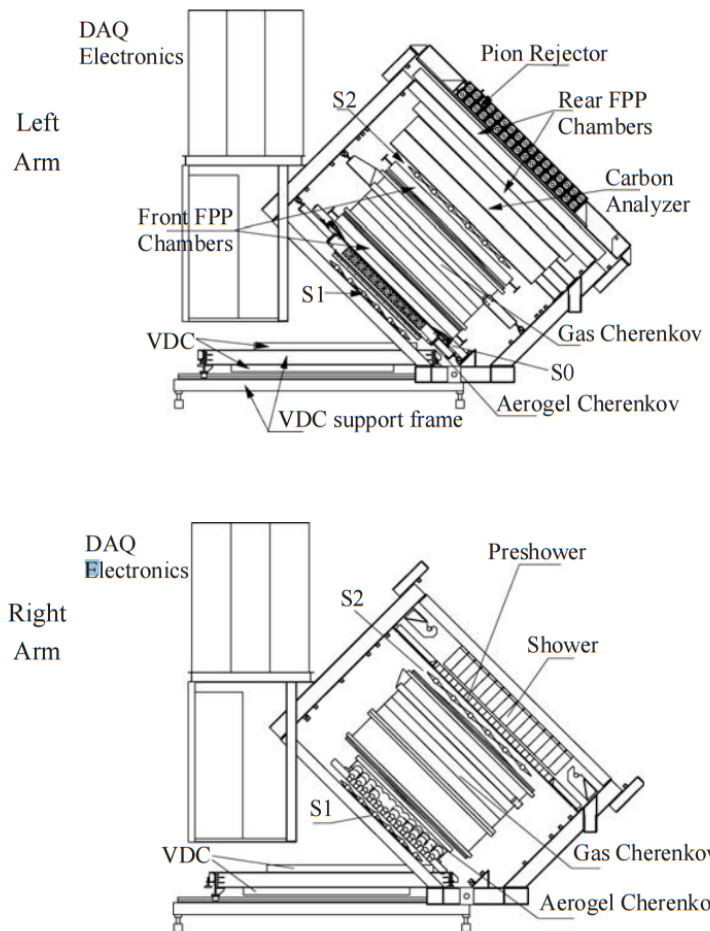


Figure 2.9: A view of both the left (top) and right (bottom) detector stacks inside the left and right HRS [1].

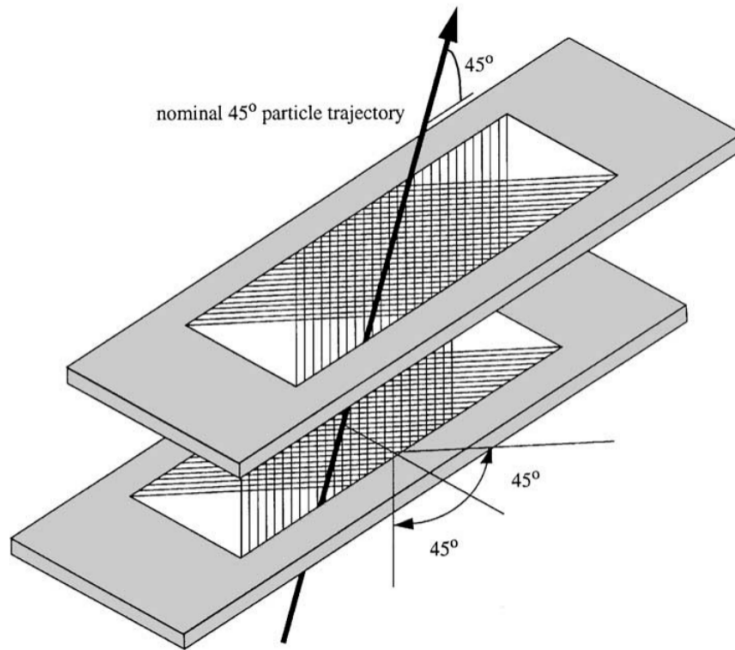


Figure 2.10: A sketch of the two VDC planes in the HRSs with a particle traveling through the detector at 45° .[6].

462 **2.3.2 Scintillators**

463 **2.3.3 Cherenkov**

464 **2.3.4 Shower Calorimeter**

465 **2.3.5 Pion Rejector**

466 **2.3.6 FPP Chambers**

467 **2.4 Trigger Setup**

468 **2.5 DAQ - Data Acquisition System**

469 **2.6 Kinematic Settings**

470 **Chapter 3**

471 **Calibration**

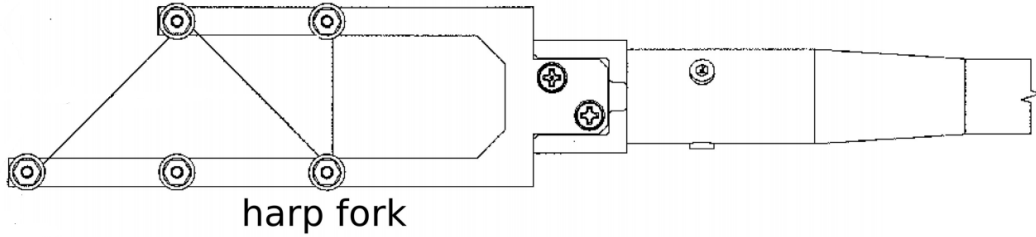
472 The information provided by the detectors originate through small changes in
473 current and voltage sent through the DAQ electronics. These signals are transformed
474 into useful information through calibration constants. The beam line elements and the
475 individual detector components were calibrate to supply highly precise and accurate
476 data.

477 **3.1 Beam Line**

478 The BPM signal coefficients are determined by a twiddle measurement. An RF
479 module attached to the BPM antennas is used to pass a signal out of each of the
480 antennas, one at a time. This will allow the determination of the conversion factor
481 for the BPM signal to relative beam position. Two harps were used to provide
482 the absolute measurement required for calibrating the BPMs. Figure 3.1 contains a
483 drawing of the harps used in Hall A. The harps were moved into the beam line when
484 calibration data is needed, but must be moved out for the production of experimental
485 data because the harp wires are intrusive to the beam operation. The harp forks are
486 aligned perpendicular to the beam line, to allow the harps to be moved in and out of
487 the beam line. Three different wires are used to determine the horizontal and vertical
488 position of the beam. Each wire has one of three orientations: vertical, sloped down

489 or sloped up. The two sloped wires are angled at 45° relative to the wire frame. As
 490 the harp fork is moved into the beam, the wires receive a signal as the beam interacts
 491 with the wires. The two sloped wires are used together to determine the vertical
 492 position of the beam. The vertical wire is used to determine the horizontal position
 493 of the beam [19, 23].

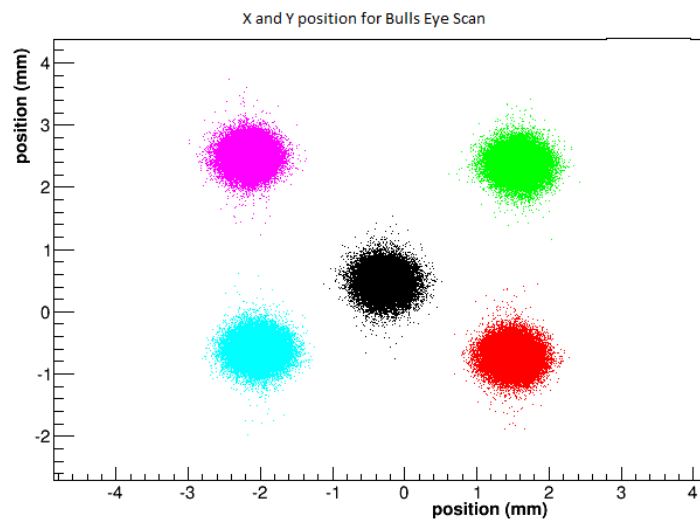
Figure 3.1: A schematic layout of a harp fork [23]



494 The location of the wires on the harp frame and the position of the harp fork
 495 were used to calculate the absolute beam position. The BPM calibration coefficients
 496 were determined by using a bulls eye scan, figure 3.2 shows an example of the five
 497 positions used to calculate the BPM calibration coefficients. The harp scan results
 498 are substituted into equation 3.1 for the X and Y positions. Using all five points and
 499 an R^2 regression technique, the coefficients can be determined with great accuracy.
 500 These highly accurate BPMs were crucial in reducing systematic error in the final
 501 results obtained from this experiment.

$$\begin{pmatrix} X_{position} \\ Y_{position} \end{pmatrix} = \begin{pmatrix} C(0, 0) & C(0, 1) \\ C(0, 0) & C(0, 1) \end{pmatrix} * \begin{pmatrix} X_{BPM} \\ Y_{BPM} \end{pmatrix} + \begin{pmatrix} X_{offset} \\ Y_{offset} \end{pmatrix} \quad (3.1)$$

Figure 3.2: The X and Y position for a Bulls eye scan for BPM calibration.



502 **Chapter 4**

503 **Data Analysis**

504 **4.1 Efficiencies**

505 The High resolution spectrometers are capable of detecting a myriad of particles
506 that track through the detectors. The designed of an experimental trigger uses the
507 properties of the individual detectors to capture data of the meaningful events. Many
508 accidentals, back ground, and unwanted events trigger the data acquisition system.
509 The removal of these unwanted events take place during analysis via software cuts.
510 Restricting the applicable signal from certain detectors through different cuts allows
511 for the rejection of back ground particles and prevents contamination in the yield
512 extraction.

513 **4.1.1 Particle Identification Efficiency**

514 One of the largest sources of contamination for the MARATHON experiment is
515 negatively charge pions. These pions are removed through software cuts made in
516 the total signal from the ten cherenkov PMTs(photomultiplier tubes) and the energy
517 deposited into the blocks of both layers of the calorimeter. Electrons can be identified
518 by their behavior in the spectrometer. High quality electrons will track through
519 the entire detector stack to deposit most of their energy into the total calorimeter

520 system and creating a large amount of light in the cherenkov. Though this knowledge
 521 tight cuts can be used to study the efficiency of the particle identification system.
 522 Plotting the signal in the cherenkov versus the energy deposited into both layers
 523 of the calorimeter allow for visual representation of the sampling cuts made in the
 524 efficiency studies, which can be seen in figure 4.1.

Cherenkov sum versus Total Energy deposited

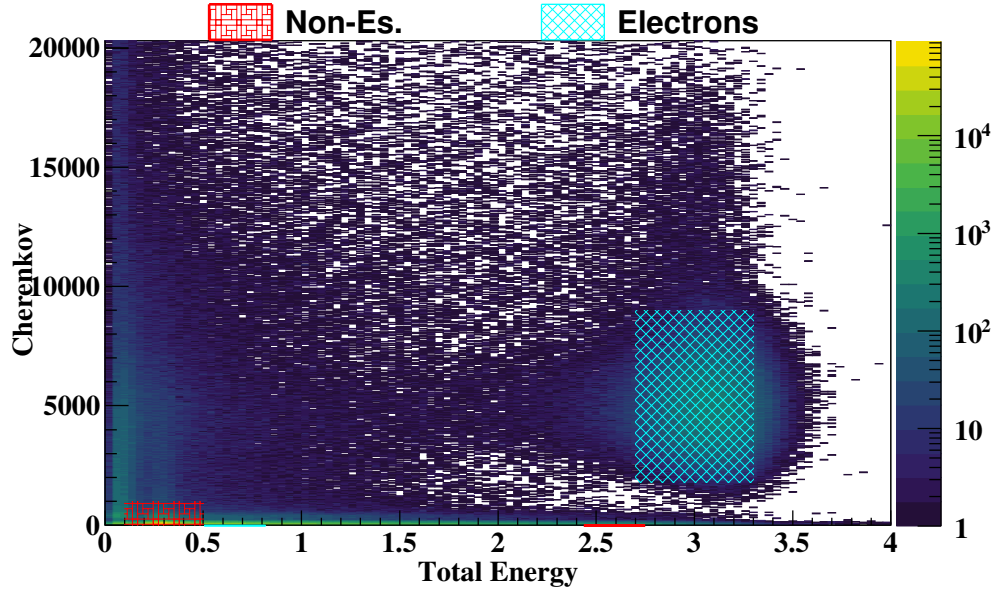


Figure 4.1: Two dimensional plot of the cherenkov sum versus Total Energy deposited, including electron sampling in teal and non-electron sampling in red.

$$GE_{sample} = \text{Known electron sample from tight cut}$$

$$GE_{pass} = GE_{sample} \text{ and pass identification cut} \quad (4.1)$$

$$Electron_{eff} = \frac{GE_{pass}}{GE_{sample}}$$

525 The efficiency of the spectrometer's particle identification(PID) detectors was
 526 determined by using the first calorimeter layer, the second calorimeter layer, and
 527 the cherenkov to provide a samples of good electrons and other particles. The PID
 528 efficiency of the individual detectors were determined using equation 4.1. The good

Particle ID and efficiency sampling for the two layers of the calorimeter

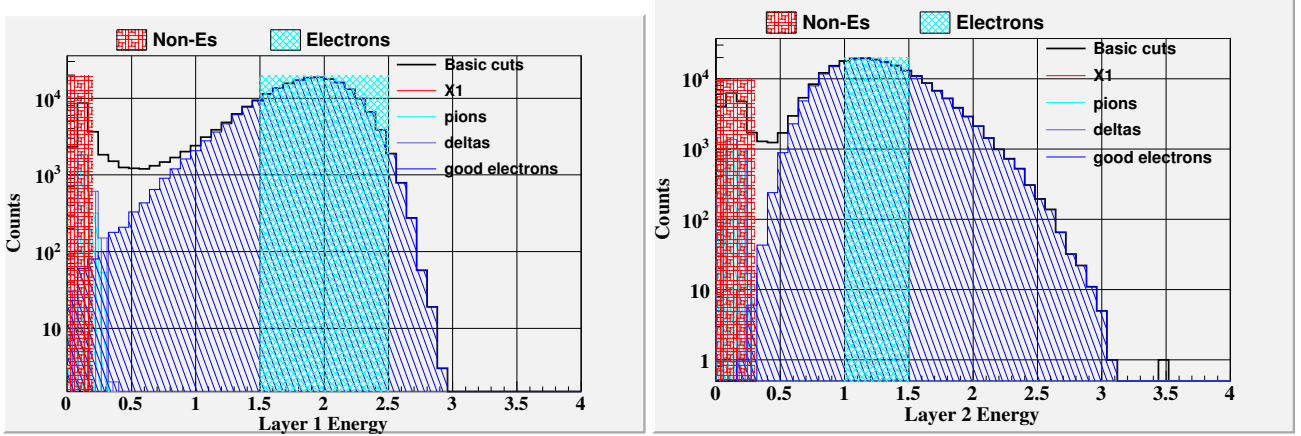


Figure 4.2: Electrons and other background particles identified via cuts in the total calorimeter and the gas cherenkov shown in the individual layers of the calorimeters. Sampling cuts for Electrons in teal and Non-Electrons in red.

529 electron sample for calculating the efficiency of the single detector was defined by
 530 sampling through the other two detectors. Sampling through the two layers of the
 531 calorimeter is shown in figure 4.2. The cherenkov good electron sample shown in figure
 532 4.3. The electron sample from the cherenkov is contaminated by delta particles that
 533 are created by secondary scattering events from pions and a combination of unknown
 534 particles titled $X1$. The $X1$ events do not deposit enough energy into the calorimeter
 535 system to be considered as good electrons that scatter from our target. Using sampling
 536 in one layer of the calorimeter and the cherenkov, these unwanted low energy particles
 537 are rejected from sampling for efficiency calculations.

Particle ID and efficiency sampling for Cherenkov

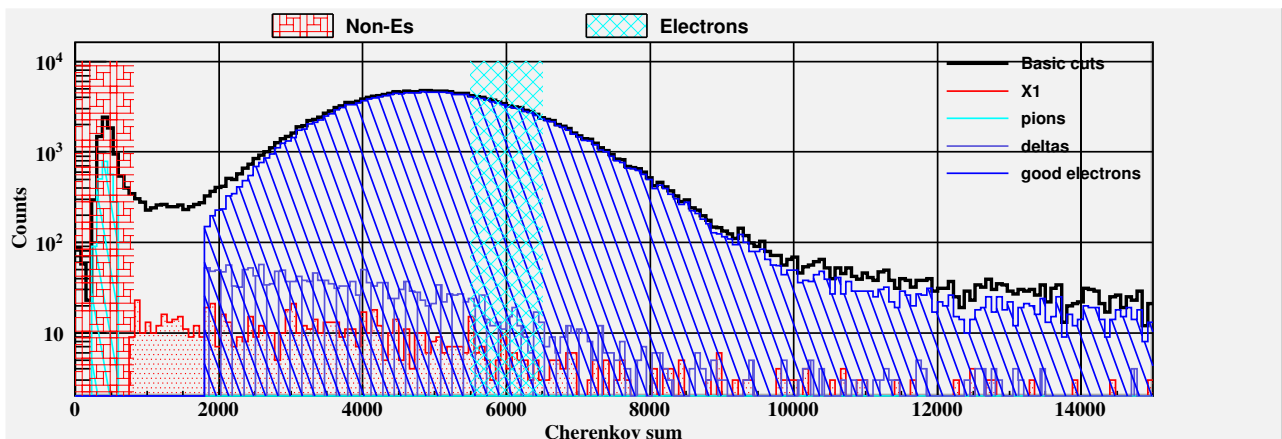


Figure 4.3: Electrons and other background particles identified via cuts in the total calorimeter and the gas cherenkov shown in the sum of the gas cherenkov. Sampling cuts for Electrons in teal and Non-Electrons in red.

⁵³⁸ Chapter 5

⁵³⁹ Results

540 **Chapter 6**

541 **Simulation**

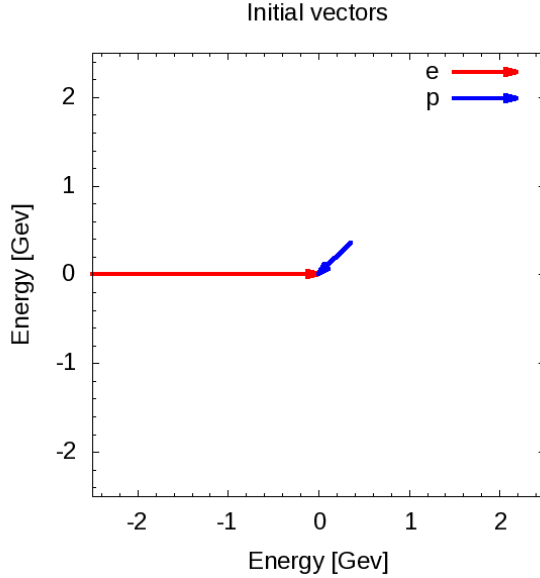
542 Nuclei are systems of nucleons that interact strongly. The characteristic scale for the
543 nucleons momentum is approximately the Fermi momentum, $k_F \approx 200 - 270 \text{ MeV}/c$
544 [9]. However because of the strongly repulsive nature of the nucleon-nucleon
545 interaction at short distances prevents two nucleons from laying in close proximately
546 to each other. This strong interaction demands the presence of high-momentum
547 components in the nuclear ground state wave function. A simulation was designed
548 to phenomenologically study the effect of these high-momentum components on the
549 nuclear EMC effect. This program was designed in two phases. The first phase used
550 simple elastic scattering and a single value for the targets momentum to investigate
551 overall effect of different target momentum on the yield in bins of x_B . The second
552 phase of the simulation was created to lay out the effect of using different momentum
553 distributions on the yield for the EMC effect region of x_B , 0.3 to 0.7.

554 **6.1 Investigation**

555 This simulation phenomenologically investigates the effect of a moving target on the
556 EMC effect by scattering a beam of electrons off of a moving proton. The target
557 protons are comprised of a directional vector of 0° to 360° in respect to the incoming
558 electron beam and a momentum between 0 and 1 GeV/c. Figure 6.1 contains a

559 possible event for the simulation. The electron approaches with 2.5 GeV of energy
560 and collides with a proton moving with a momentum of 0.5 GeV/c with an angle of
45° in respect to the electron trajectory.

Figure 6.1: Example of the electron beam(red) with a energy of 2.5 GeV and the proton(blue) with angle of 45° in respect to the electron and with a momentum of 0.5 GeV/c.



561
562 Using conservation of momentum and conservation of energy in elastic collisions,
563 this simulation calculates the final state of the electron and proton after the scattering
564 event by randomly selecting a scattered direction for the electron. The vector
565 representation of the scattered products are shown in figure 6.3a. In order to
566 make these calculations systematic and to study cross sections models the simulation
567 transform each event into the rest frame of the target before scattering.

568 6.2 Transformation

569 The Simulation completes a set of Lorentz invariant rotations and boost for each
570 event to transform the lab frame of the electron and proton collision into the rest
571 frame of the proton. First the simulation takes the initial proton and electron vectors

572 and rotates them to align the proton vector to the horizontal axis, shown in figure
 573 6.2b. This rotation uses the angle between the proton and the electron defined as λ .
 574 This allows for a straight forward calculations for the Lorentz factors β and γ and
 575 to boost into the rest frame of the target proton, figure 6.2c. Once in the boosted
 576 frame, the angle between the electron and the horizontal axis is defined as δ . Right
 577 before the simulation starts to calculate the scattered products, it completes one more
 578 rotation to align the electron vector with the horizontal axis, figure 6.2d, to make the
 579 scattering calculation systematic and unconditional.

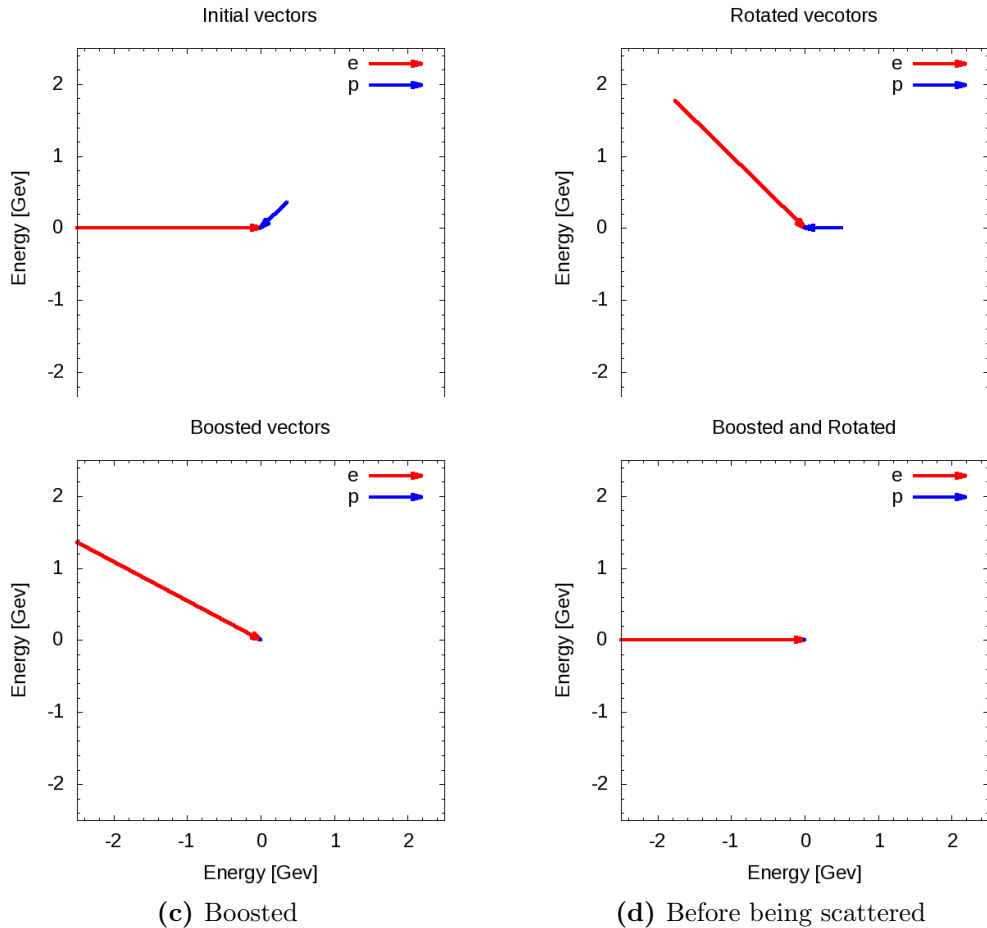


Figure 6.2: Vector representations of the momentum for the incoming electron(red) and target proton(blue) with units of GeV for each phase of their transformations before scattering.

580 In order to gain a more complete understanding of the scattering products, the
581 program completes a set of transformations to move from the rest frame of the target
582 proton to the beginning lab frame. After the simulation calculates the scattered
583 products it begins to transform back by beginning with a rotation by the angle δ ,
584 figure 6.3b. Followed by the inverse of the previously used Lorentz boost. The
585 last transformation, a rotation by λ , transforms the frame back into the lab frame.
586 A proton vector and electron vector in the lab frame are the final products of the
587 simulation. An image of the electron and proton vectors for each transformation can
588 be found in figure 6.3. These vectors allow for calculation of kinematic variables such
589 as Bjorken x and the four-momentum transfer (Q^2). This simulation will complete
590 these steps for many electron and proton combinations.

591 6.3 Results

592 This electron scattering simulation produced results for two stages. The firsts stage
593 used a fix proton momentum for each run to compare the yield in bins of x_B . Figure
594 6.4 shows the results for three different runs, each having a unique fixed proton
595 momentum. The red histogram represents a run with a proton momentum of 0 Gev/c.
596 The result is an elastic peak at x_B of one. The blue histogram contains the results
597 having a fixed proton momentum of 0.25 GeV/c. Increasing the initial momentum
598 of the proton spreads the events into two peaks. The scattering interactions that
599 form the peak above 1 x_B are produced by events were the proton's initial directional
600 vector are orientated towards the electron. The events that produce an x_B below
601 1 have a proton direction pointing away from the electron initially. Doubling the
602 proton's initial momentum from 0.25 GeV to 0.50 GeV causes these peaks two spread
603 out furtherer in x_B .

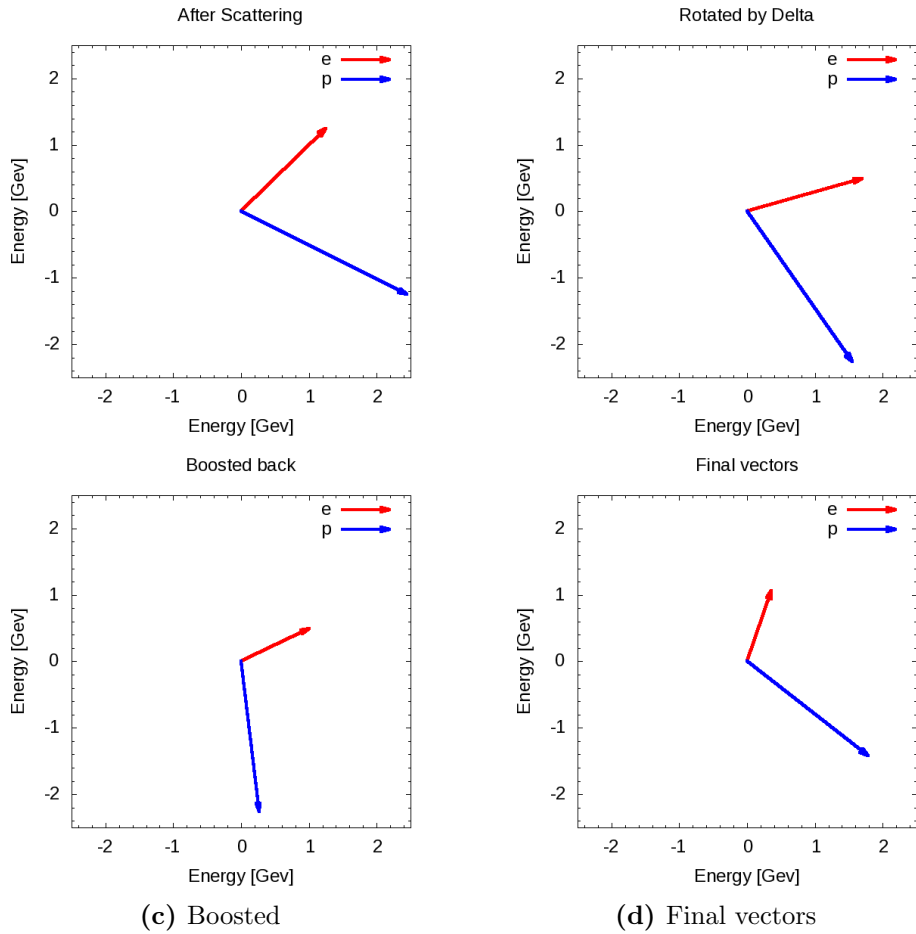
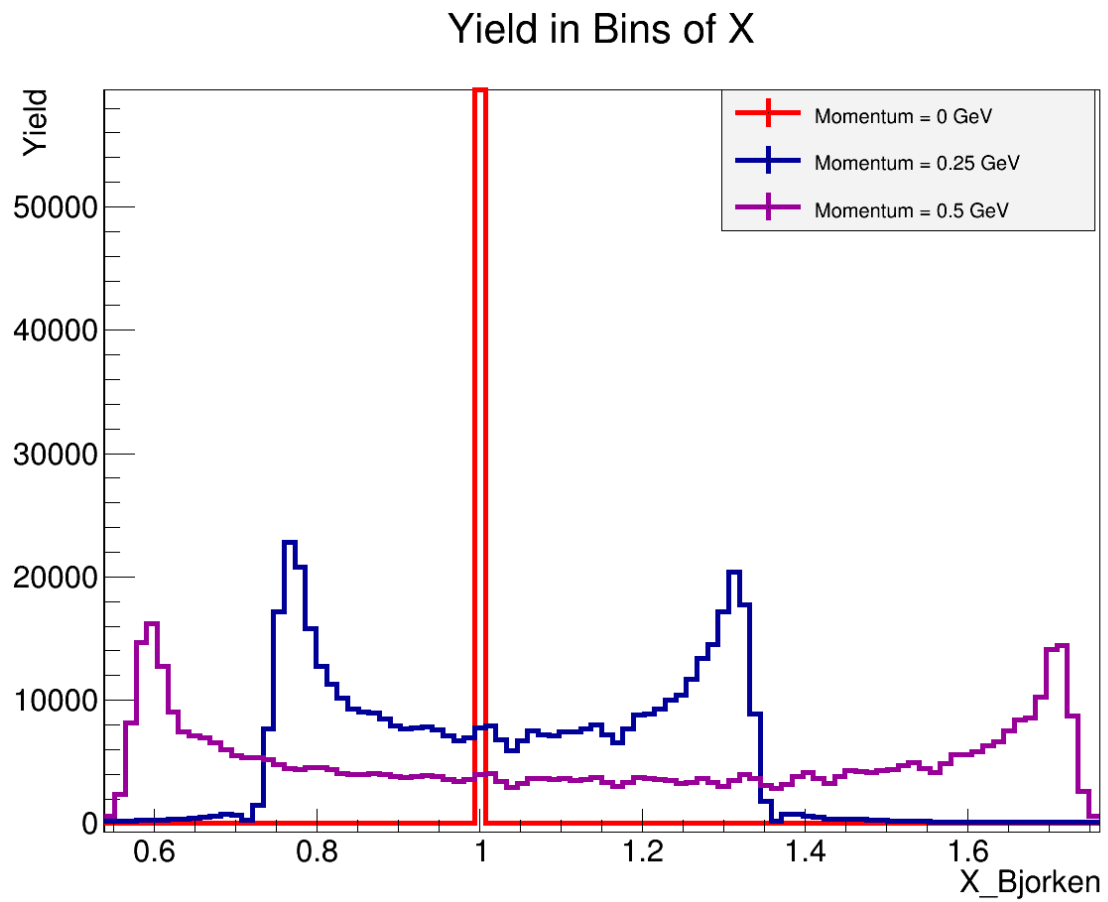


Figure 6.3: Vector representations of the momentum for the incoming electron(red) and target proton(blue) with units of GeV for each phase of their transformations after scattering).

Figure 6.4: Simulation results for fixed momentum protons. Three runs with unique proton momentum.



604 Chapter 7

605 Conclusion

Bibliography

607

Bibliography

- 608 [1] J. Alcorn et al. Basic Instrumentation for Hall A at Jefferson Lab. *Nucl. Instrum.*
609 *Meth.*, A522:294–346, 2004. [vi](#), [11](#), [12](#), [13](#), [19](#), [20](#), [21](#)
- 610 [2] John Arrington, Aji Daniel, Donal Day, Nadia Fomin, Dave Gaskell, and Patricia
611 Solvignon. A detailed study of the nuclear dependence of the EMC effect and
612 short-range correlations. *Phys. Rev.*, C86:065204, 2012. [8](#)
- 613 [3] A. Daniel, J. Arrington, and D. Gaskell. Measurements of the EMC effect in
614 few-body nuclei at large x. *AIP Conf. Proc.*, 1369:98–105, 2011. [9](#)
- 615 [4] J. Denard and J. Sahar. High accuracy beam current monitor system for cebaf’s
616 hall a. Chicago, 2001. Particle Accelerator Conference. [vi](#), [16](#), [17](#)
- 617 [5] J. Edelmann, G. Piller, Norbert Kaiser, and W. Weise. Resonances and higher
618 twist in polarized lepton nucleon scattering. *Nucl. Phys.*, A665:125–136, 2000. [8](#)
- 619 [6] K.G. Fissum et al. Vertical drift chambers for the hall a high-resolution
620 spectrometers at jefferson lab. *Nuclear Instruments and Methods in Physics*
621 *Research Section A: Accelerators, Spectrometers, Detectors and Associated*
622 *Equipment*, 474(2):108 – 131, 2001. [vi](#), [20](#), [22](#)
- 623 [7] David J. Flay. *Measurements of the Neutron Longitudinal Spin Asymmetry A1n*
624 *and Flavor Decomposition in the Valence Quark Region*. PhD thesis, Temple
625 University, Philadelphia, PA, Aug 2014. [vi](#), [2](#), [3](#), [16](#)

- 626 [8] D.F. Geesaman, K Saito, and A Thomas. The nuclear emc effect. *Annual Review*
627 *of Nuclear and Particle Science*, 45(1):337–390, 1995. [8](#)
- 628 [9] J. Gomez et al. Measurement of the A-dependence of deep inelastic electron
629 scattering. *Phys. Rev.*, D49:4348–4372, 1994. [8, 31](#)
- 630 [10] D. Higinbotham. The emc effect still puzzles after 30 years - cern courier.
631 <http://cerncourier.com/cws/article/cern/53091>, April 2013. (Visited on
632 01/04/2016). [vi, 2, 7, 9](#)
- 633 [11] Doug Higinbotham. Target images, December 2017. [18](#)
- 634 [12] R Hofstadter. Nuclear and nucleon scattering of high-energy electrons. *Annual*
635 *Review of Nuclear Science*, 7(1):231–316, 1957. [4](#)
- 636 [13] Henry W. Kendall. Deep inelastic scattering: Experiments on the proton and
637 the observation of scaling. *Rev. Mod. Phys.*, 63:597–614, Jul 1991. [6](#)
- 638 [14] Simona Malace, David Gaskell, Douglas W. Higinbotham, and Ian Cloet. The
639 Challenge of the EMC Effect: existing data and future directions. *Int. J. Mod.*
640 *Phys.*, E23:1430013, 2014. [6](#)
- 641 [15] R. W. McAllister and R. Hofstadter. Elastic scattering of 188-mev electrons from
642 the proton and the alpha particle. *Phys. Rev.*, 102:851–856, May 1956. [2](#)
- 643 [16] David Meekings. Hall a tritium target. Thomas Jefferson Lab, Virginia,
644 engineering Report, 2017. [17](#)
- 645 [17] P R Norton. The emc effect. *Reports on Progress in Physics*, 66(8):1253, 2003.
646 [vi, 8](#)
- 647 [18] Bogdan Povh, Klaus Rith, Christoph Scholz, and Frank Zetsche. *Particles and*
648 *Nuclei: An Introduction to the Physical Concepts*. Springer, 2009. [1, 2, 4, 5, 6](#)

- 649 [19] Tom Powers, Lawrence Doolittle, Rok Ursic, and Jeffrey Wagner. Design,
650 commissioning and operational results of wide dynamic range bpm switched
651 electrode electronics. *AIP Conference Proceedings*, 390(1):257–265, 1997. [13](#),
652 [24](#)
- 653 [20] J. Seely et al. New measurements of the european muon collaboration effect in
654 very light nuclei. *Phys. Rev. Lett.*, 103:202301, Nov 2009. [2](#), [9](#)
- 655 [21] Richard E. Taylor. Deep inelastic scattering: The early years. *Rev. Mod. Phys.*,
656 63:573–595, Jul 1991. [6](#)
- 657 [22] Hall A Tech. Ep method. [http://hallaweb.jlab.org/equipment/beam/
658 energy/ep_web.html](http://hallaweb.jlab.org/equipment/beam/energy/ep_web.html). (Accessed on 06/28/2016). [16](#)
- 659 [23] Pengjia Zhu et al. Beam Position Reconstruction for the g2p Experiment in Hall
660 A at Jefferson Lab. *Nucl. Instrum. Meth.*, A808:1–10, 2016. [vi](#), [13](#), [14](#), [15](#), [24](#)

Appendix

661